Korean J. Chem. Eng., 38(9), 1923-1933 (2021)
DOI: 10.1007/s11814-021-0813-5

pISSN: 0256-1115
eISSN: 1975-7220

Unified NCNT@rGO bounded porous silicon composite as an anode material for Lithium-ion batteries

Arunakumari Nulu, Venugopal Nulu, Ji Seong Moon, and Keun Yong Sohn†

Department of Nanoscience and Engineering, Center for Nano Manufacturing, Inje University,
197 Inje-ro, Gimhae, Gyeongnam-do 50834, Korea
(*Received 28 December 2020 • Revised 26 March 2021 • Accepted 18 April 2021*)

Abstract–Nano/micro silicon particles were achieved by high energy ball milling of silicon mesh powder as a cheap and scalable process and used to make porous silicon by acid etching. Subsequent dispersing of porous silicon with nitrogen-doped carbon nanotubes and graphene oxide followed by filtration and heat treatment gives the composite of unified structures of NCNT@rGO protected porous silicon. The obtained composite was studied as an anode material for Li-ion batteries, and it delivered a high reversible capacity of 862/861 mAh g^{-1} at 200 mA g^{-1} with 91% of capacity retention. Along with superior rate capability, the prepared composite exhibited 578 and 451 mAh g^{-1} discharge capacity at 1,000 and 2,000 mA g^{-1} after a long 300 cycles. The enhanced electrochemical performance of the composite electrode can be accredited to the highly conductive and tough matrix of NCNT@rGO blend structures, and porosity in silicon effectively controls the silicon expansion and accommodates the required buffer volume during lithiation/de-lithiation.

Keywords: Porous Silicon, Silicon/Carbon Composite, NCNT@rGO Structures, Composite Anodes, Li-ion Batteries

INTRODUCTION

Silicon is one of the most investigated anode materials for lithium-ion batteries (LIBs) owing to its high theoretical capacity of 3,572 mAh g^{-1} and low working potential vs. Li/Li^+ [1-3]. However, the massive volume expansion (~300%), low electronic conductivity, and unstable solid electrolyte interphase (SEI) layer formations are the main drawbacks that hinder the practical application of silicon (Si) anodes. During lithium reactions, active silicon material undergoes cracking that eventually leads to loss of contact with the current collector, resulting in decline in capacity and poor electrochemical performance [3-6]. Several strategies have been undertaken to address these issues, such as reducing the silicon particle size and making different structures to control the particle cracking and pulverization [7-10]. Fabrication of porous and hollow structures of materials to accommodate the required buffering volume that allows easy diffusion of electrolyte during lithium alloying [11,12]. Making composites with carbon matrix to increase the electric conductivity and structural integrity is the most effective way to advance silicon-based anodes materials [13-15]. Recently, improved binders and electrolytes [16-18], different types of yolk-shell structures [19-21], etc., are the other ways to improvise silicon electrodes for LIBs.

As mentioned, different silicon nanostructures and nano-designs deliver better electrochemical properties. Schulz et al. synthesized silicon nanowire anode by electrospinning method [22]. Park et al. synthesized carbon-coated Si nanotubes by chemical deposition method [23]. Chan et al. grew silicon nanowires by the CVD process [24], Fleischauer et al. prepared silicon nanopillars by thermal evaporating technique [25]. However, large-scale material production is impractical due to the necessity for sophisticated equipment and high synthesis costs. Moreover, most of the Si-based anodes, such as Si/C composites, porous structures are derived from highly expensive Si nanoparticles as a precursor that limit practical industrial application. Additionally, unsafe HF etching is needed to remove unwanted SiO_x layer on the surface of Si nanoparticles [26,27]. Preparation of nano/micro/sub-micron Si particles from bulk Si using a high energy ball milling is a cost-effective approach to overcome Si nanoparticle production cost [28-30]. Nevertheless, massive volume changes and low conductivity make it challenging for pure Si to stand as an efficient anode to deliver long and stable cycle life for Li-storage applications. In this view, comprehensive approaches have been developed, such as silicon anodes combined with carbon matrix to afford structural stability, mechanical flexibility, and high electrical conductivity.

High conductivity, large surface area, high thermal stability, and flexibility of carbon nanotubes (CNTs) have received much attention as a combination of high capacity silicon anodes [31,32]. The composite anodes from Si and CNT aim to take advantage of the respective electrochemical and physical properties of each component [33-35]. Gohier et al. synthesized Si decorated vertically aligned CNTs anode, exploiting the collective merits of CNTs and silicon. The perfect adhesion between CNTs and silicon particles facilitated electron and lithium-ion transport pathway and led to 800 mAh g^{-1} capacity recovery at 10C [36]. To further improve the composite of Si and CNTs, Cui and team synthesized freestanding CNT-Si films up to 4 μm thickness by a CVD process, which are successfully integrated the current collector and anode active material into a single sheet of film. These films delivered an excellent cycling performance with 2,000 mAh g^{-1} charge storage capacity due to good

†To whom correspondence should be addressed.
E-mail: ksohn@inje.ac.kr

mechanical strength and conductivity of the CNT network and high energy capacity due to the use of Si as anode material and maintained structural integrity upon repeated lithium insertion and extraction [37]. It is evident that nitrogen-doping into carbon material significantly increases electrical conductivity and shortens Li^+ diffusion length, consequently highly beneficial for long cyle and superior rate performance [38-40]. However, these Si/CNT or C composite electrodes initially show better cyclability; later, gradual fading in capacity was observed due to their structural destruction, and losing CNTs or C binding with Si and caused poor cyclability [41-43]. Therefore, additional improvement is needed to maintain the structural stability of such composites. For that purpose, reduced graphene oxide (rGO) drew our attention owing to its excellent mechanical and electrical properties [44]. The rGO additive to Si/CNT or Si/C could effectively afford enough void space to accommodate the volume changes of Si during Li^+ reactions and also assure good electric contact and mechanical stability to the composite material [45,46].

Based on these findings and considering relatively low-cost and scalable production processes, we proposed unified structures of nitrogen-doped carbon nanotubes @ reduced graphene oxide (NCNT@rGO) protected porous Si composite anode for LIBs. The porous Si particles in the composite are embedded in highly conductive and flexible NCNT/rGO unified structures. These structures give the required buffer volume for Si expansion and maintain their structural integrity during the lithiation/de-lithiation process and deliver stable cyclability with highly reversible capacity after 100 cycles.

EXPERIMENTAL

1. Materials and Methods

Si powder (325 mesh, 99% trace metals basis, Sigma Aldrich), aluminum nitrate nonahydrate (DAEJUNG, 1036-4405), melamine (DAEJUNG, 5652-4100), multi-walled carbon nanotubes (CNT) (Hanwha Nanotech Corp. CM-100, diameter: 10 nm-14 nm), and ethanol solvent (Sigma-Aldrich, ≥99.5%) were purchased and used without further purification.

2. Material Preparation

The three components in the composite material, porous silicon (pSi), nitrogen-doped carbon nanotubes (NCNT), and graphene oxide (GO), were obtained separately by a physical and chemical approach described below and used to prepare the final composite material pSi/NCNT@rGO.

2-1. Fabrication of Porous Nano/Micro Si

The preparation process of porous Si is as follows. 3 g of Si powder (325 mesh) was taken into a high-energy ball milling high-density polyethylene (HDPE) vial along with a few zirconium balls, with a ball to powder mass ratio of 50 : 1. Then the vial was closed and placed in a ball mill. Then milling was carried out for 48 h at room temperature. After, the obtained Si powder with zirconium-balls was sieved about 1 h and the powder collected, referred to as mesh Si-48. Then 6.7 g of Aluminium nitrate (Si to aluminum weight ratio 1 : 1) was dissolved in a few ml of DI water and allowed for complete dissolution by magnetic stirring. Then 500 mg of mesh Si-48 was added to it and sonicated for 30 min. This process was followed by magnetic stirring for 2 h to make a uniform suspension. The obtained suspension was oven-dried at 100 °C. The obtained dried sample was heat-treated in a tube furnace at 600 °C for 3 h with a heat-rate of 4 °C per min in an argon atmosphere to get aluminum-doped Si. The obtained powder was immersed with a 3 M HCl solution for etching for about 6 h with magnetic stirring. The solid material was separated by centrifugation and washed with DI water. After that, the obtained sample was dried in the oven for 6 h to get porous Si (pSi).

2-2. Preparation of N-doped CNTs

N-doped CNTs were prepared by dissolving 400 mg of melamine into hot water and mixed well until becoming a uniform solution.

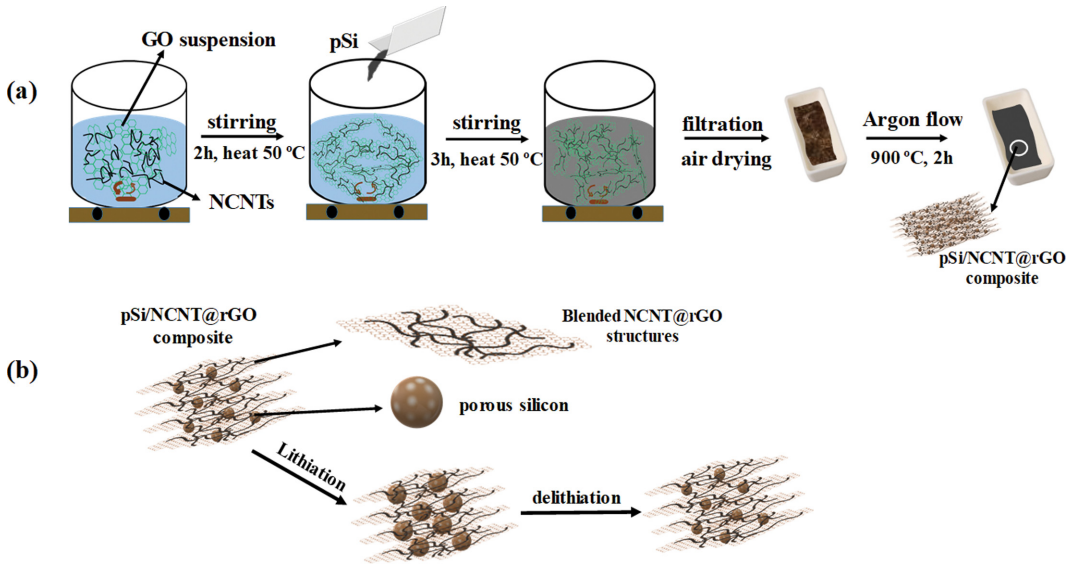

Fig. 1. (a) The schematic illustration of the synthesis procedure of the pSi/NCNT@rGO composite, (b) schematic representation showing the structural and volumetric changes of pSi/NCNT@rGO during lithiation and delithiation process.

Then 200 mg of CNTs was added and magnetic stirring was carried out for 2 h at low heating on a hot-plate. The thickened mixture was air-dried in the oven. Later, the dried sample was heat-treated in N_2 atmosphere at 800 °C for 1 h. After heat treatment, the sample was collected and referred to as NCNT.

2-3. Preparation of pSi/NCNT@rGO

Graphene oxide (GO) was prepared using the modified Hummers method [41,42]. A schematic illustration of the synthesis strategy of pSi/NCNT@RGO is shown in Fig. 1(a). 400 mg of GO was exfoliated in distilled water and stirred for a few minutes to form a stable GO suspension. Then 100 mg of N-CNT was added to the GO suspension and magnetically stirred for 2 h to blend well. We added 200 mg of pSi powder and continued the stirring process for 3 h. Later, we carried out vacuum filtration to the suspension, collected the suspended solid material, and air-dried it in the oven. The dried sample was heat-treated in an argon atmosphere at 900 °C for 2 h with a heat-rate of 4 °C per min. After the annealing process, the material was collected and named as pSi/NCNT@rGO composite. The expected closer view of the structures and volume/structural changes during lithiation/de-lithiation are shown in Fig. 1(b). For the comparison study, the same experimental conditions were used to prepare pSi/NCNT composite without GO suspension.

3. Chemical Analysis and Characterization Techniques

The prepared composite's crystallinity was examined by X-ray diffraction with Cu K radiation (λ=1.5406 A°). Raman spectroscopy was employed to analyze the chemical composition of the sample. Scanning electron microscopy (SEM) and transmission electron microscopy (TEM) were used to characterize the prepared sample structures and morphology. Thermogravimetric analysis (TGA) was employed from 25 °C to 800 °C. Brunauer-Emmett-Teller (BET), Barrett, Joyner, and Halenda (BJH) methods were applied to analyze the specific surface area and pore size distribution of our prepared samples.

4. Electrochemical Analysis

All electrochemical tests were carried out by using the BioLogic battery testing instrument. 2032R type coin type half-cells were used to evaluate the electrochemical performance of prepared electrodes. All working electrodes were prepared by 70% active material with 15% of super P carbon conductive additive and 15% of polyamide-imide (PAI) in N-methyl pyrrolidone binder. All electrode components were well mixed by mini-milling, and the resultant slurry was coated on a copper foil with uniform thickness. The dry electrode was then placed in a vacuum oven at 200 °C for 3 h to activate the binder. After that, the dried-electrode was punched into 14 mm discs and used as a working electrode. The calculated mass loading of active material on the punched electrode was ~1.4 mg cm^{-2}, with an average thickness of 160 μm. Metallic lithium was employed as a counter electrode, 1 M $LiPF_6$ in ethylene carbonate, diethyl carbonate, and fluoroethylene carbonate with a v/v ratio 5 : 70 : 25 as an electrolyte and polypropylene film as a separator. All cells were fabricated in an argon-filled glove box and examined between the voltage window of 0.01-2.0 V. The cyclability was measured at 200 mA g^{-1}, and rate capability was measured from 200 to 3,200 mA g^{-1} applied current densities. The electrode's redox behavior was analyzed using cyclic voltammetry (CV) in the voltage range of 0.01-2.0 V at a scan rate of 0.1 mV s^{-1}. Electrochemical impedance spectroscopy (EIS) was conducted within the frequency range of 10 mHz to 10 kHz. The specific capacity of the working electrode was determined based on the weight of the active material.

RESULTS AND DISCUSSION

Fig. 2(a) shows the XRD patterns of prepared mesh Si-48, pSi/NCNT, and pSi/NCNT@rGO samples. The sharp diffraction peaks at 2θ=28.4°, 47.4°, 56.2°, 69.2°, and 79.5° correspond to the (111), (220), (311), (400), and (331) lattice planes of prepared samples and are well-consistent with pristine Si, indicating that no structural changes had occurred after high-temperature heat treatment [13, 14]. The sharp peak at 25.8° in pSi/NCNT corresponds to C(002) of NCNT. The two weak and broad peaks at 26° and 43.6° in pSi/NCNT@rGO are attributed to (002) and (101) crystal planes of NCNT@rGO. No peak was observed at 10.5° respective to GO, indicating the successful reduction of GO [45,46]. The XRD patterns of CNT and NCNT are shown in Fig. S1. The peaks at 25.7° and 43° represent (002) and (100) planes of carbon. After N-doping, the peak intensities are decreased, but the overall peak position remain the same in the NCNT sample, indicating no possible side reactions during the doping process.

The elemental composition of the prepared samples was investigated by Raman spectroscopy, and the results are shown in Fig. 2(b). The peak at 520 cm^{-1} is Si's characteristic peak exhibited by mesh Si-48, pSi/NCNT, and pSi/NCNT@rGO samples. However, the peak positions of pSi/NCNT (516 cm^{-1}) and pSi/NCNT@rGO (508 cm^{-1}) have shifted towards the lower wavelength. A similar

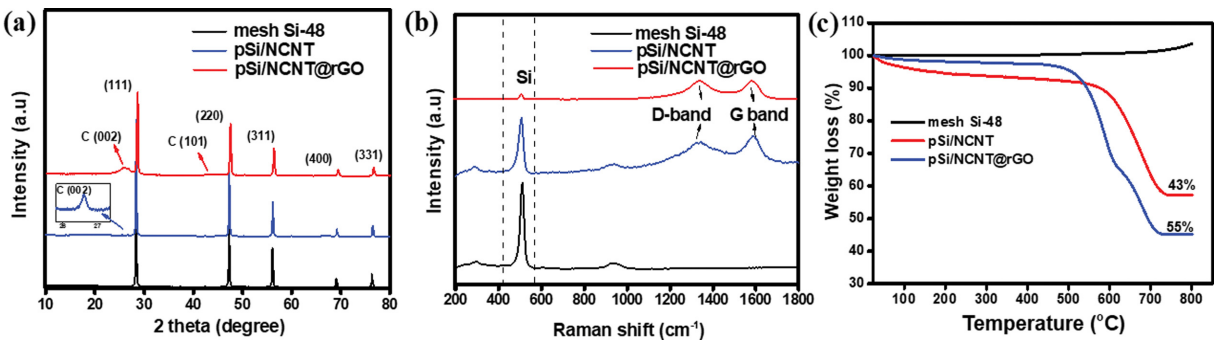

Fig. 2. (a) XRD patterns, (b) Raman spectra, (c) TGA results of obtained mesh Si-48, pSi/NCNT, pSi/NCNT@rGO.

effect has also been observed in previous literature [45,46]. This phenomenon could be due to the NCNT@rGO blend, which covers the Si particles, indicating the composite's successful formation. Two broad peaks at 1,335 cm^{-1} and 1,596 cm^{-1} in pSi/NCNT, and pSi/NCNT@rGO correspond to the D band and G band, ascribed to the presence of structural defects and graphitic carbon, respectively. The I_D/I_G ratio gives information about the nature of the carbon in the composite. The I_D/I_G of pSi/NCNT@rGO (1.1) is higher than that of pSi/NCNT (0.85), which represents the NCNT@rGO blend has high structural defects and can afford excellent electric conductivity and be beneficial for faster Li^+ diffusion reactions [47,48].

Thermogravimetric analysis was carried out from 25 °C to 800 °C, to determine the amount of carbon present in the prepared samples, and weight loss (%) vs. temperature plots are depicted in Fig. 2(c). There is no considerable weight loss in mesh Si-48, indicating no carbon in that sample. But it shows a gradual increase in weight after 500 °C, due to the conversion of Si into SiO_x. But pSi/NCNT and pSi/NCNT@rGO show significant weight loss after 500 °C. The calculated weight loss was 43% and 55% for pSi/NCNT and pSi/NCNT@rGO, respectively. The weight loss is attributed to the oxidation of carbon in the air. We believe that the composite's carbon content can provide excellent conductivity, and buffering volume to Si substantially improves the overall electrochemical performance of the material [30,45].

The samples' microstructures were evaluated through SEM, and the resultant images are displayed in Fig. 3. The SEM image of mesh Si-48 is shown in Fig. 3(a), and the particles are of different sizes ranging from 100 nm (white arrows in the inset) to a few micrometers (red arrows) are observed. The porous structure of Si after Al etching is shown in Fig. 3(b). The successful formation of porous Si with different pore size (shown with yellow arrows) is found, and these porous structures help ease the volume effect of Si during lithium reactions. Fig. 3(c) and 3(d) are the SEM images of prepared pSi/NCNT@rGO composite at different magnification, and the images reveal that unified NCNT@rGO well bounds the pSi particles.

To further confirm, the structural morphology of prepared pSi/NCNT@rGO was investigated by TEM images and shown in Fig. 4. As shown in Fig. 4(a) and 4(b), Si particles are well surrounded by NCNT@rGO and form 3D morphology, which effectively maintains structural integrity and stable morphology. The inset shows the enlarged view of a specified part from Fig. 4(b), and the plane spacing 0.31 nm ascribed to (111) plane of Si, indicating its highly crystalline nature in the composite. The unified structure of NCNT@rGO is further confirmed by image Fig. 4(c), in which both CNTs and rGO are well associated and form a super-tough, flexible, and highly conductive matrix. These structures support pSi to accommodate buffer volume and afford required electric conductivity and protect from pulverization throughout the electrochemical reactions with lithium. The HR-TEM of a specified part in Fig. 4(c) is depicted in Fig. 4(d). The two planes with spacing 0.33 nm and 0.34 nm are attributed to the (002) planes of NCNT and rGO, hence confirming their existence in the composite material. The EDX elemental mapping was done to know the elemental distribution in the prepared composite, and the results are displayed in Fig. 4(e). From Fig. 4(e), the pSi particle is well surrounded by the unified carbon blend. The doped-N in CNTs also is uniformly distributed in the carbon blend and helps in faster Li^+ diffusion. From the results of

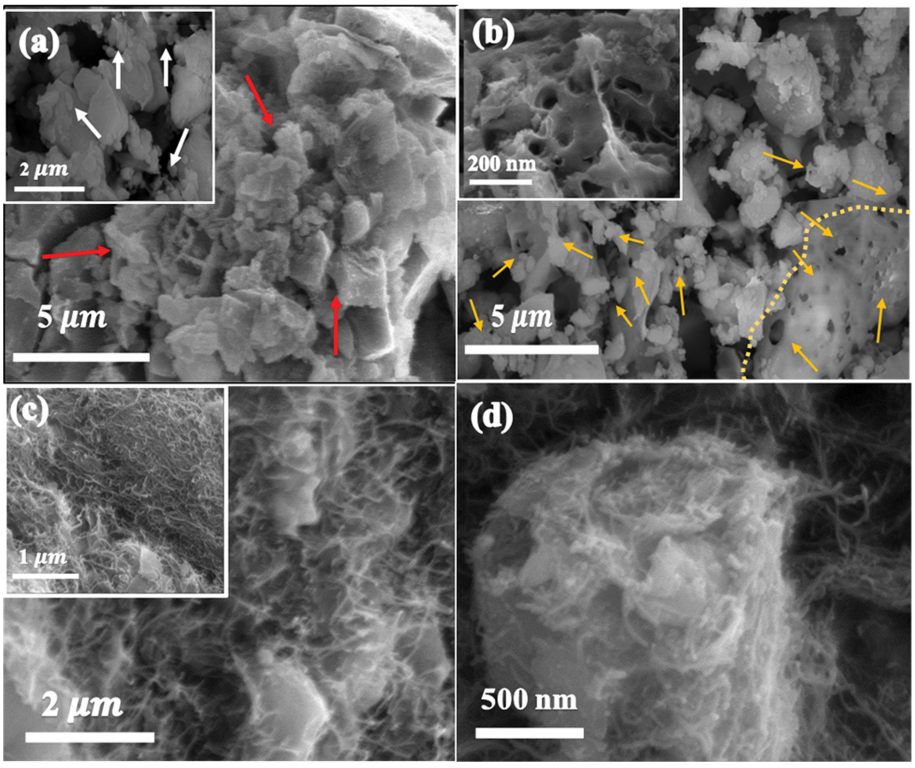

Fig. 3. SEM images of (a) mesh Si-48, (b) pSi, (c) pSi/NCNT@rGO, (d) magnified view of pSi/NCNT@rGO.

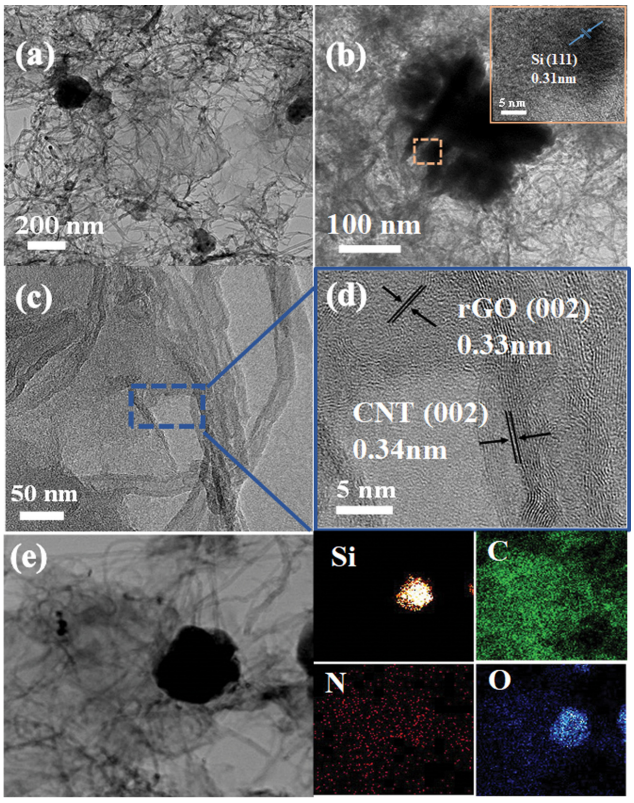

Fig. 4. TEM images of (a) pSi/NCNT@rGO (b) magnified view of pSi/NCNT@rGO (inset shows the (111) plane of Si) (c) unified NCNT/rGO matrix (d) HR-TEM image of a specific part from (c), shows (002) planes of rGO and CNT respectively. (e) TEM image and the corresponding elemental mapping of the pSi/NCNT@rGO.

SEM and TEM, the prepared composite has an arrangement of core pSi particles, surrounded by NCNT@rGO matrix, and these results are in good agreement with the XRD, SEM, and TEM results.

To analyze the pSi/NCNT@rGO composite's surface chemical states, XPS was employed, and the results are shown in Fig. S2. The detected elements Si, C, N, and O are shown in the survey scan spectrum Fig. S2(a). The curve-fitting procedure was used to distinguish the chemical states of Si, C, and N. As shown in Fig. S2(b), the Si 2p spectrum has fitted into three peaks related to Si-Si bonding at 99.5 eV, Si-C bonding at 100.5 eV. The third peak at 103.5 eV is related to SiO_x, the partial oxidation layer of the Si surface. This oxidation could be possible during the heat treatment process [48]. C 1s spectrum, shown in Fig. S2(c), contains two peaks assigned to C-C bonding at 284.6 and C-O bonding at 286.1 eV. The high-resolution spectrum of N 1s is depicted in Fig. S2(d) and consists of three peaks. The peaks at 398.2 eV and 400 eV are related to pyridinic and pyrrolic N, respectively. The other peak at 402.2 eV is assigned to graphitic N. The N 1s spectrum further confirms N's presence in the composite and improving the conductivity and Li-ion diffusion of the electrode material [38,39]. Fig. S2(e) shows the O 1s spectrum with a peak at 532.6 eV attributed to O-Si bonding from SiO_x. These results are well consistent with the TEM elemental mapping results.

The nitrogen adsorption-desorption isotherms at 77 K, and the pore-size distribution curves are shown in Fig. S3. From Fig. S3(a), according to the IUPAC classification, nonporous type II isotherms are shown by mesh Si-48, and pSi/NCNT and mesoporous type IV isotherms are shown by pSi and pSi/NCNT@rGO. The pore width, pore-volume, and BET surface areas are significantly increased from mesh Si-48 to pSi due to porosity. However, the surface area of pSi/NCNT is decreased due to the blocking of the pores by NCNTs. This is evident by the decrease in the pore volume of pSi from 0.275 $cm^3 g^{-1}$ to pSi/NCNT 0.228 $cm^3 g^{-1}$. For the pSi/NCNT@rGO composite, the BET surface was significantly increased compared with the pSi sample and possessed a higher number of pores in the mesoporous region. This phenomenon could be due to the presence of rGO in the material [49,50]. The increased surface area improves Li^+ kinetics, and mesopores allow fast penetration of electrolytes and control the mechanical stress in the pSi/NCNT@rGO composite electrode. The pore volume, surface area, and average pore widths of all samples are summarized in Fig. S3(c).

We applied different electrochemical tests to evaluate the performance of the prepared composite electrode pSi/NCNT@rGO. We also tested mesh Si, mesh Si-48, and pSi/NCNT electrodes under the same conditions for a comparison study. The CV results of pSi/NCNT@rGO, mesh Si, mesh Si-48, and pSi/NCNT for the first five cycles are shown in Fig. 5(a), S4(a), (b), and (c), respectively. In the first lithiation of the cathodic scan, mesh Si and mesh Si-48 electrodes show a distinct reduction peak around ~0.65 V resulting from the decomposition reaction of electrolyte and formation of SEI layer. But compared with mesh Si and mesh Si-48, the prepared pSi/NCNT and pSi/NCNT@rGO materials show wide, broad reduction peaks between 1.6-0.3 V and demonstrate a greater extent of SEI layer formation. The possible reason for this large SEI layer in the later electrodes is the availability of a much larger surface area in the composites due to NCNT and NCNT@rGO matrix. As a result, pSi/NCNT and pSi/NCNT@rGO have much more electrolyte/electrode interfacial areas to encourage the electrolyte decomposition reaction and the SEI layer formation [45]. The two other sharp peaks at ~0.19 V and ~0.05 V vs. Li/Li^+ are observed in all electrodes and related to lithium's alloying reaction into crystalline Si and evaluation of metastable amorphous Li_xSi phases. For anodic scan, peaks at ~0.34 V and ~0.51 V vs. Li/Li^+ for both pSi/NCNT@rGO and pSi/NCNT are the characteristic peaks of the two-step dealloying of the Li_xSi phase to amorphous Si, respectively. This phenomenon is commonly observed in many Si-based anodes. However, only one anodic peak at 0.55 V vs. Li/Li^+ appears for both mesh Si and mesh Si-48 electrodes, indicating the dealloying in these electrodes is a slow and sluggish process. The intensities of two-dealloying anodic peaks in pSi/NCNT@rGO and pSi/NCNT are increased and become sharper, indicating that the dealloying kinetics process has dramatically improved after the introduction of carbon materials [48,51,52]. The oxidation peaks gradually increase from the first cycle to the fifth cycle, which is related to the ongoing activation process of the electrode materials [51].

The increased peak intensity in the subsequent cycles is related to the gradual activation process of the electrodes. Moreover, the

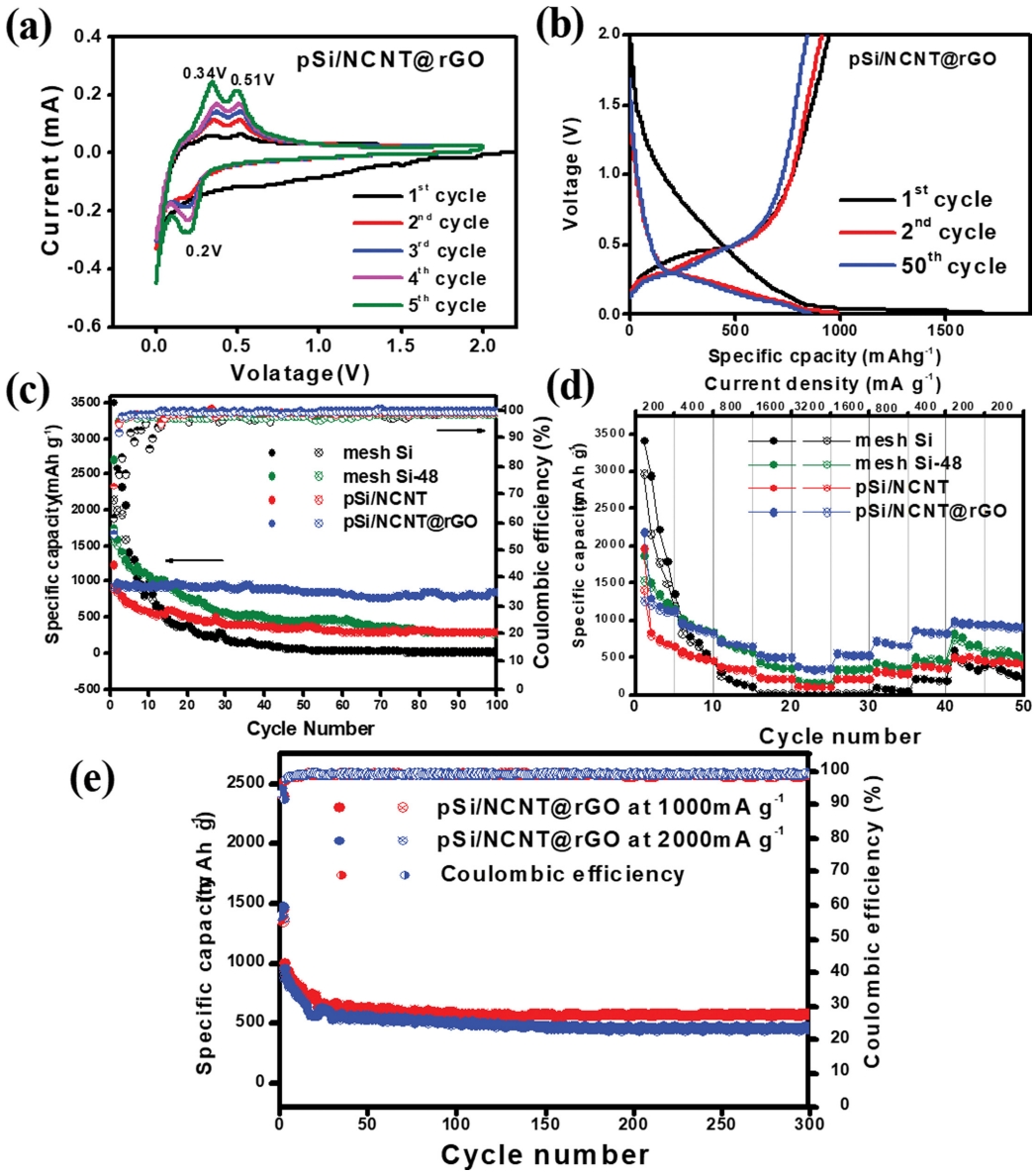

Fig. 5. (a) Cyclic voltammograms of the first five cycles of pSi/NCNT@rGO (b) charge and discharge voltage profiles of pSi/NCNT@rGO for the 1st, 2nd, and 50th cycles, (c) cyclability and coulombic efficiency results, (d) rate capability result of mesh Si-48, pSi/NCNT and pSi/NCNT@rGO electrodes, (e) cycling behavior and Coulombic efficiency of pSi/NCNT@rGO composite at high applied current densities of 1,000 mA g^{-1} and 2,000 mA g^{-1}.

anodic peaks of pSi/NCNT@rGO are shifted to lower potential, while the cathodic peaks are shifted to higher potential, demonstrating the faster Li^+ kinetics compared with mesh Si, mesh Si-48, and pSi/NCNT electrodes. This increment in Li^+ kinetics and wettability of pSi/NCNT@rGO composite electrode result from the excellent conductivity afforded to Si by the unified structure of NCNT@rGO [51,52]. The voltage vs. charge/discharge capacity profiles of pSi/NCNT@rGO, mesh Si, mesh Si-48, and pSi/NCNT electrodes for 1st, 2nd, and 50th cycles at a current density of 200 mA g^{-1} are displayed in Fig. 5(b), S4(d), (e) and (f), respectively. The long discharge plateau below 0.1 V in the first cycle in all electrodes represents the alloying reaction of lithium with crystalline Si and the Li_xSi phase formation. In the following cycles, the discharge plateaus are shifted to ~0.25 V due to the typical Si transformation from crystalline to amorphous. The long charge plateau above 0.5 V represents the de-alloying process of the Li_xSi phase to amorphous Si [31,32]. These charge/discharge profiles are in good agreement with their respective CV results. The first discharge/charge capacities of mesh Si, mesh Si-48, pSi/NCNT, and pSi/NCNT@rGO are 3,514/2,159 mAh g^{-1}, 2,719/1,574 mAh g^{-1}, 1,238/904 mAh g^{-1}, and 1,689/944 mAh g^{-1} with CEs of 61%, 57.8%, 73%, and 56%, respectively. The irreversible capacity loss is associated with the SEI layer formation on the electrode's surface. The lower initial coulombic efficiency (ICE) for pSi/NCNT@rGO could be ascribed to the decomposition of electrolyte and accumulation of Li^+ ions by the blend NCNT@rGO carbon matrix. But in the second cycle, the

CE of pSi/NCNT@rGO reaches 92% with 988/911 mAh g^{-1} specific capacities, which is a good sign of high reversible performance. The CE is gradually increased with cycling and stabilized above 98% for all electrodes. After 50 cycles, the electrodes pSi/NCNT@rGO, pSi/NCNT, mesh Si-48 and mesh Si exhibited specific capacities, about 869/866 mAh g^{-1}, 370/367 mAh g^{-1}, 446/437 mAh g^{-1}, and 62/60 mAh g^{-1}, respectively. These results indicated that the protected unified structures play a crucial role in maintaining the structural integrity of pSi and acted as conductive support, and benefitted in attaining stable capacities [47,51].

To evaluate the changes in ICE values and specific capacity, we prepared three other composite materials with different pSi, NCNT@rGO ratios such as 55 : 45, and 63 : 35, and 75 : 25 and cycled for 50 charge/discharge cycles at 200 mA g^{-1} current density, and the resulting graph is displayed in Fig. S5. From the results, the discharge/charge capacity at first cycle for electrodes with pSi and NCNT@rGO ratios 45 : 55, 55 : 45, and 63 : 35, and 75 : 25 is 1,689/944 mAh g^{-1}, 1,791/1,086 mAh g^{-1}, 2,016/1,307 mAh g^{-1} and 2,544/1,499 mAh g^{-1} with ICEs of 56%, 60.6%, 63.8%, and 58.9%, respectively. From the results, the initial coulombic efficiency of the composites was increased with lessening the amount of carbon in the composite. However, more Si in the sample (75 : 25) could undergo massive volume expansion and result in irreversible capacity loss, resulting in lower initial coulombic efficiency (58.5%). After 50 cycles, the composites exhibit 869/866 mAh g^{-1}, 908/899 mAh g^{-1}, 964/959 mAh g^{-1}, and 730/725 mAh g^{-1} specific capacity with 92%, 83%, 73.7%, 48% of capacity retention compared with the first reversible capacity. Thus, we conclude that increased carbon content in the composite material decreases the initial coulombic efficieny due to the accumulation of more Li^+ ions in its first cycle. However, the carbon improves the cyclic stability and capacity retention by giving good electric conductivity, structural stability, and buffering volume to core pSi particles. The same typical behavior of Si/C-based composite anodes is also observed in the previous reports [53,54].

The long cyclability and respective CE results of mesh Si, mesh Si-48, pSi/NCNT, and pSi/NCNT@rGO electrodes are shown in Fig. 5(c). In the initial cycles, mesh Si exhibited higher specific capacities compared with the other three electrodes. However, these capacities declined rapidly with increasing cycling. After 100 cycles, the mesh Si electrode delivered specific capacity of 16/15 mAh g^{-1} with <1% capacity retention. The massive capacity loss of this electrode is mainly due to large volume changes during lithium insertion/extraction reactions, leading to particle pulverization and loss of contact with the current collector. On the other hand, mesh Si-48 delivered better performance than mesh Si. The results could be due to nano/micro-size particles, which can reduce particle pulverization to some extent. After 100 cycles, the electrode exhibits its specific capacity of 288/284 mAh g^{-1}, with 18% of capacity retention. Conversely, pSi/NCNT, and pSi/NCNT@rGO composite electrodes delivered better specific capacity than the other two electrodes. After 100 cycles, pSi/NCNT and pSi/NCNT@rGO composite electrodes delivered specific capacity of 306/304 mAh g^{-1} and 862/861 mAh g^{-1} with capacity retention of 34%, 91%, respectively. These results indicate that N-doped CNTs are insufficient to provide structural stability to pSi and the need for rGO matrix. The unified structure of NCNT@rGO in the composite successfully afforded excellent conductivity, structural flexibility to core pSi, maintaining its structural integrity and forming a stable SEI layer during the long cycling process. N-doping, porosity in Si, also helped in faster Li^+ diffusion into the active material and advantageous for achieving stable and long cyclability. The rate capability of pSi/NCNT@rGO was evaluated along with pSi/NCNT, mesh Si-48, and mesh Si electrodes at a wide range of applied current density from 200 to 3,200 mA g^{-1} in the voltage window of 0.01-2.0 V, and the results are depicted in Fig. 5(d). As increasing the applied current density, the specific capacities are decreased. Among all, pSi/NCNT@rGO electrode stands out and exhibited higher specific capacity of 2,182, 965, 721, 535, 382 mAh g^{-1} at 200, 400, 800, 1,600, and 3,200 mA g^{-1} current density. After gradually decreasing the applied current density from 3,200 mA g^{-1} to 200 mAg^{-1}, the electrode retained 964 mAh g^{-1} discharge capacity indicating excellent structural stability of pSi/NCNT@rGO electrode. On the other hand, the mesh Si electrode failed at 1,600 mA g^{-1} current density, and capacity reached zero where mesh Si-48 and pSi/NCNT electrodes delivered 147 mAh g^{-1} and 95 mAh g^{-1} at 3,200 mA g^{-1}, respectively. The rate capability results suggest that the combination of NCNT and rGO played a significant role in providing electrical conductivity and structural flexibility. Moreover, the tough matrix of NCNT@rGO effectively prevents the escape of small active silicon particles, which gives more active sites to lithium.

Additionally, the core porous silicon can accommodate substantial volume changes during the charge/discharge process. Fig. 5(e) shows the long cyclability of pSi/NCNT@rGO electrode at high current density of 1,000 and 2,000 mA g^{-1}. The electrode-specific capacity gradually decreased at the initial cycles, but after 20 cycles, the capacity stabilized. After a long 300 cycles, the electrode delivered 578/574 mAh g^{-1} and 451/449 mAh g^{-1} specific capacity at respective 1,000 and 2,000 mA g^{-1} applied current density. These results indicate the excellent cyclic stability of the electrode, even at higher current density.

The interfacial property between electrode and electrolyte was analyzed by employing EIS. The resultant Nyquist plot results for mesh Si-48, pSi/NCNT, and pSi/NCNT@rGO electrodes before and after ten charge/discharge cycles at 200 mA g^{-1} are depicted in Fig. 6(a) and 6(b), respectively, and the equivalent circuit model for the fitted curves is displayed in Fig. 6(c). From the Nyquist plots, all electrodes exhibited semicircle at the middle and high-frequency region corresponding to the charge transfer resistance at the interface of electrode and electrolyte and a straight line at the low-frequency region associated with a lithium diffusion process [55,56]. The equivalent circuit model in Fig. 6(c) consists of solution resistance (R_s), SEI layer resistance (R_{SEI}), charge transfer resistance (R_{ct}), constant phase elements (CPE_1, CPE_2), and Warburg impedance (W_b). As shown in Fig. 6(a), mesh Si-48 shows a semicircle with a large diameter, indicating higher charge transfer resistance (469 Ω) due to the low conductivity Si. However, the charge-transfer resistance pSi/NCNT (43 Ω) and pSi/NCNT@rGO (56 Ω) electrodes are significantly lower than the mesh Si-48 electrode, showing that making a composite of Si with carbon can effectively enhance the transfer of electrons and charges. After ten cycles, R_{ct} values of all electrodes are further decreased to lower resistance

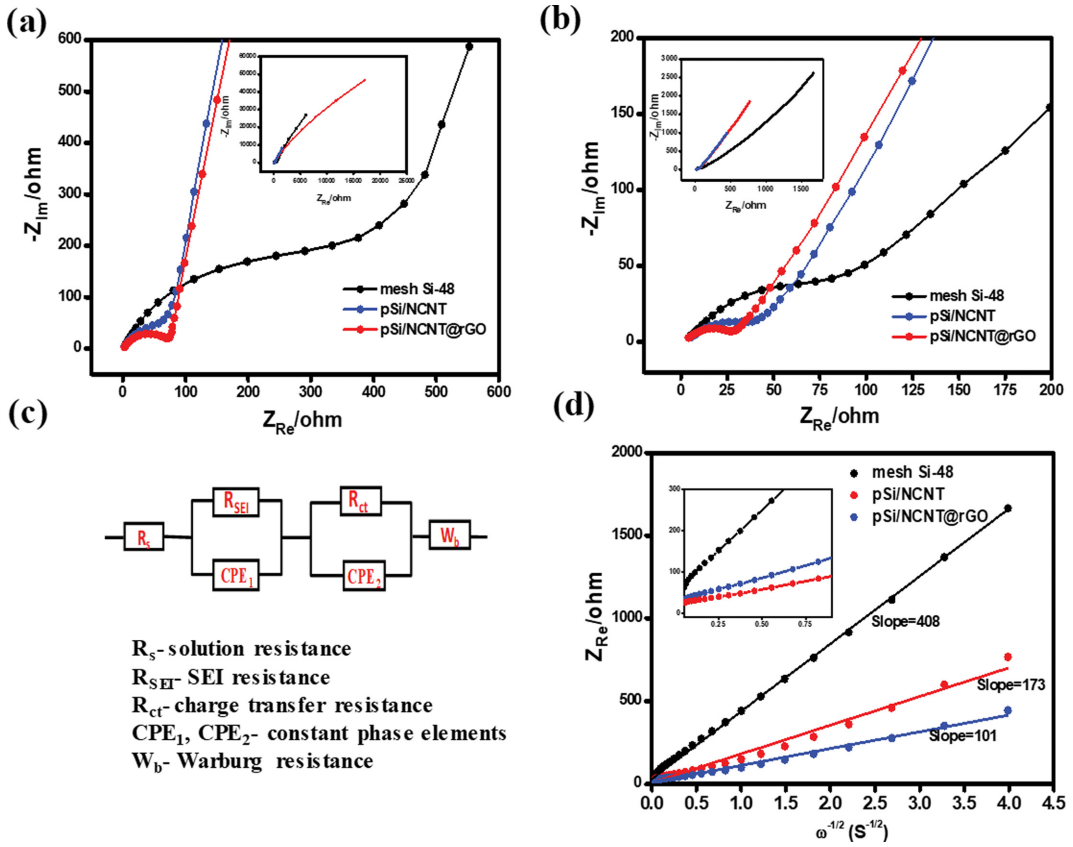

Fig. 6. EIS spectra of mesh Si-48, pSi/NCNT, and pSi/NCNT@rGO electrodes (a) before cycling (b) after ten cycles (c) equivalent circuit model for fitting curves (d) Z_{Re} vs. $\omega^{-1/2}$ plots at low-frequency region.

values considerably due to the improved electrode kinetics. Among the three electrodes, the pSi/NCNT@rGO electrode showed less R_{ct} value, indicating a good sign of lithium kinetics of the active material. The R_{SEI} of the pSi/NCNT@rGO electrode is also much smaller than pSi/NCNT and mesh Si-48 electrodes, indicating the stable SEI layer formation, which is also advantageous in getting higher specific capacity and long cycle life. The R_{ct} value of mesh Si-48 is significantly reduced due to the slow wetting process of the electrolyte into electrodes and the increase in the conductivity of the electrode after lithium-ion reactions, indicating the enhanced kinetics during the initial cycles. But from Fig. 5(c), the specific capacity values of mesh Si-48 declined from the 1st to 10th cycle, resulting from the unstable SEI layer formation and large volume expansion of the Si electrode [15]. R_s, R_{SEI}, and R_{ct} values before and after ten cycles are summarized in Table 1. The Z_{Re} vs. $\omega^{-1/2}$ plots

Table 1. Summarized impedance values with calculated diffusion coefficients

Sample	R_s (ohm) BC/AC	R_{SEI} (ohm) BC/AC	R_{ct} (ohm) BC/AC	D (cm^2s^{-1})
mesh Si-48	2.6/4	89/30	469/62.4	8.68×10^{-14}
pSi/NCNT	4.2/1.5	49.6/17	43/32	4.83×10^{-13}
pSi/NCNT@rGO	4.1/2.3	41/13	56/22	1.41×10^{-12}

*BC-before cycling, AC-after 10 cycles

of all three electrodes are shown in Fig. 6(d), where Z_{Re} linearly depends on $\omega^{-1/2}$ in the low-frequency region. The below equations were used to estimate the diffusion coefficient of Li^+ (D).

$$Z_{Re}=R_s+R_{SEI}+R_{ct}+\sigma_w\omega^{-1/2} \quad (1)$$

$$D=R^2T^2/2A^2F^4C^2\sigma_w^2 \quad (2)$$

Here, R is the gas constant, T is the absolute temperature, C is the molar concentration of Li^+ ions, A is the electrode area, and F is the Faraday constant. The Warburg impedance coefficients σ_w can be calculated from the slope of Z_{Re} vs. $\omega^{-1/2}$ plots. The calculated Warburg factors for mesh Si-48, pSi/NCNT, and pSi/NCNT@rGO are 408, 173, and 101, respectively. From Eq. (2), the lower Warburg factor will give a higher diffusion coefficient. The diffusion coefficient for all electrodes (after ten cycles) was calculated from Eq. (3) and shown in Table 1. The results show that the pSi/NCNT@rGO electrode shows much-improved lithium diffusion than the other two electrodes. The higher D_{Li+} indicates faster kinetics of the cell reactions in the pSi/NCNT@rGO electrode due to high conductivity and shorter Li^+ and electron transporting lengths, resulting from the NCNT/rGO blend and porous Si structures in the composite electrode [48].

The SEM images of electrodes before and after cycling were tested to quantitatively evaluate the thickness change of the electrode. Fig. 7(a) and (b) show the cross-sectional SEM images of the pSi/NCNT@rGO electrode before and after cycling. The pSi/

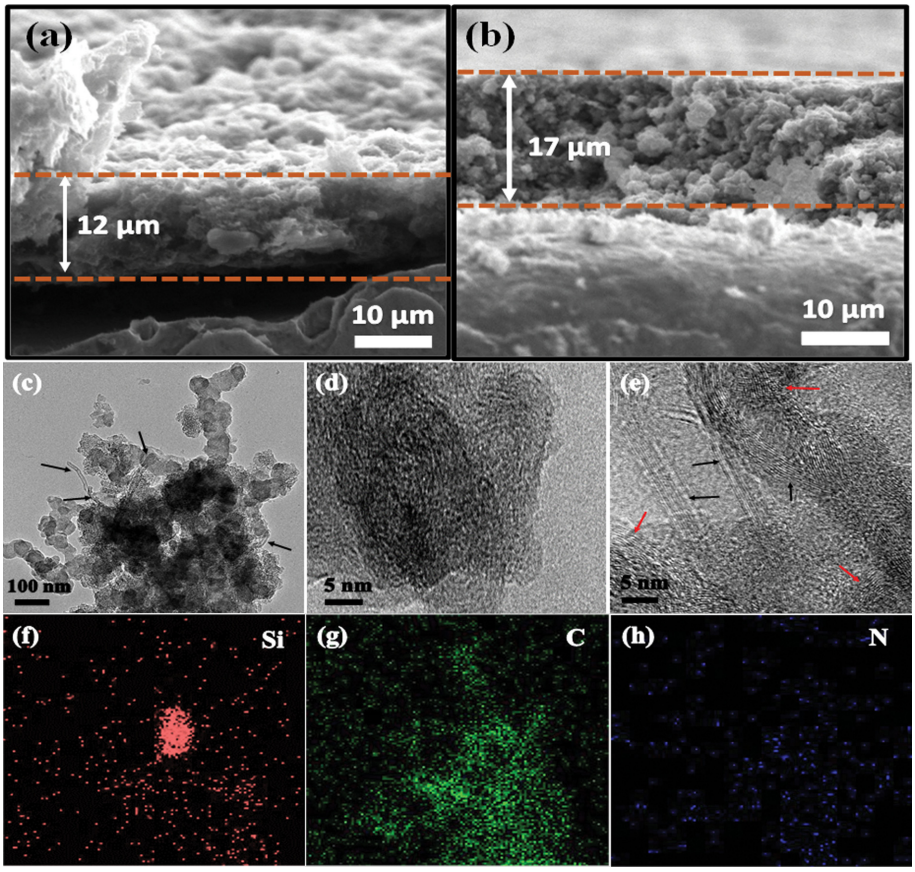

Fig. 7. SEM cross-sectional view of pSi/NCNT@rGO electrodes (a) before cycling, (b) after 100 cycles. (c) TEM image of pSi/NCNT@rGO composite after 10 cycles. (d) and (e) HR-TEM images of silicon and NCNT@rGO matrix, respectively. (f), (g) and (h) are corresponding EDX elemental mapping of Fig. 7(c).

NCNT@rGO electrode with a thickness of 12 µm exhibited a thickness increase of 41.6% (17 µm) after 100 cycles and maintained the electrode integrity. Moreover, the cycled electrode did not show any signs of disintegration and cracking. These results indicate that the unified structure of NCNT@rGO successfully controls the large volume expansion of Si particles during the cycling process. The morphology changes of the pSi/NCNT@rGO composite electrode after ten cycles were inspected by TEM characterization. Before the analysis, the cycled electrode was carefully disassembled in the glove box and washed with anhydrous dimethyl carbonate several times to remove the SEI layer. Then the electrode was air-dried and the electrode material carefully collected. The TEM image of the cycled pSi/NCNT@rGO composite material is shown in Fig. 7(c), and corresponding HR-TEM images of Si and unified NCNT@rGO are shown in Fig. 7(d) and (e). As shown in Fig. 7(c), pSi particles are still bounded by the unified NCNT@rGO structure. Some NCNT were found and are indicated by black arrows. The HR-TEM images of Si in Fig. 7(d) did not show any crystalline planes due to silicon particle amorphization during the cycling process. Alternatively, the HR-TEM image of the NCNT@rGO blend from Fig. 7(e) still shows some crystalline planes of CNTs and rGO. The EDX elemental mapping of image Fig. 7(c) is shown in Fig. 7(f), (g), and (h) corresponding to Si, C, N mappings. From the elemental mapping results, it can be seen that the pSi particles are well surrounded by an N-doped carbon matrix blend and protected from structural destruction, and helped in maintaining structural integrity.

The practical applicability of pSi/NCNT@rGO electrode in the LIBs was evaluated by making a full-cell battery with commercially available $LiCoO_2$ (LCO) cathode and pre-lithiated pSi/NCNT@rGO anode. The full cell was investigated with a cut-off voltage of 2.80-4.20 V. The fundamental electrochemical properties, such as cycling, rate performance, and charge/discharge profiles of the LCO cathode, are shown in Fig. S6. The excellent cycle stability and rate capability of the LCO cathode suggest that it can be a good candidate for full-cell fabrication. Before constructing a full cell, the N/P ratio was fixed at 1.2 to avoid differences in the electrode material capacity. For comparison study, two other full-cells with N/P ratios of 0.95 and 1.1 were also prepared and tested with the same conditions. The pre-lithiated composite anode was used as a working electrode for full-cell fabrication after its first lithiation to 0.01 V at 200 mA g^{-1}. The charge/discharge profiles and excellent cyclability with coulombic efficiency data are included in Fig. 8(a) and 8(b), respectively. The full-cell exhibits a specific capacity of 88/87 mAh g^{-1} at 0.5 C (1 C=140 mA g^{-1}, based on the cathode active material) with a capacity retention of 70% after 50 cycles. The full-cell comprising pSi/NCNT@rGO//LCO affords a reasonable energy density of 308.5 Wh kg^{-1} with an average voltage of 3.5 V, which

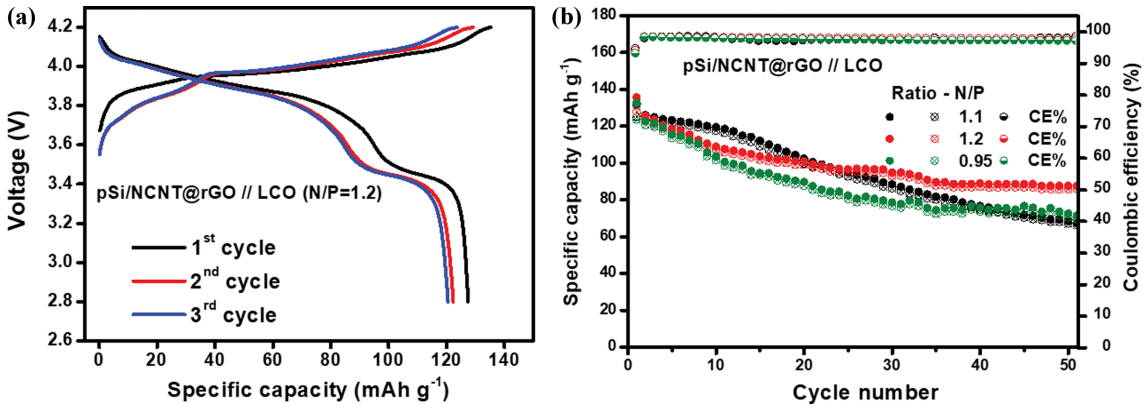

Fig. 8. (a) Charge/discharge profiles for the 1st, 2nd, and 3rd cycles, (b) cyclability and coulombic efficiency results of assembled full-cell with pSi/NCNT@rGO and $LiCoO_2$ as anode and cathodes at different N/P ratios.

are promising results from composite prepared from cost-effective mesh Si, CNT, and GO for Li^+ ion energy storage applications.

CONCLUSION

We successfully prepared nano/micro-size porous silicon embedded in the NCNT@rGO matrix by employing a cost-effective and scalable approach. In the prepared composite, silicon's porosity helps to penetrate electrolytes into the electrode material. The robust and endurable NCNT@rGO matrix collectively provides conductivity, structural stability, and buffering volume to core porous silicon particles. These key factors favor the composite electrode to achieve 91% capacity retention after 100 cycles. The excellent mechanical stability and high conductivity afforded by the unified NCNT@rGO matrix are accountable for the composite's long-term cyclability. The full-cell fabricated from the composite anode and $LiCoO_2$ cathode delivered 88 mAh g^{-1} capacity with an energy density of 308.5 Wh kg^{-1}. We believe that the successful fabrication of our composite material using a low-cost and convenient approach benefits the development of next-generation advanced battery materials and represents a promising pathway for practical applicability.

ACKNOWLEDGEMENTS

This research was funded by grants (NRF-2018R1D1A1B07044026 and NRF-2015R1D1A1A01059983) from the Basic Science Research Program through the National Research Foundation of Korea (NRF), which is funded by the Ministry of Education.

SUPPORTING INFORMATION

Additional information as noted in the text. This information is available via the Internet at http://www.springer.com/chemistry/journal/11814.

REFERENCES

1. M. N. Obrovac, L. Christensen, D. B. Le and J. R. Dahn, *J. Electrochem. Soc.*, **154**, A849 (2007).
2. L. Baggetto, R. A. H. Niessen and P. H. L. Notten, *Electrochim. Acta*, **54**, 5937 (2009).
3. M. Ashuri, Q. He and L. L. Shaw, *Nanoscale*, **8**, 74 (2016).
4. X. Zuo, J. Zhu, P. M. Buschbaum and Y. J. Cheng, *Nano Energy*, **31**, 113 (2017).
5. Y. Sun, N. Liu and Y. Cui, *Nat. Energy*, **1**, 16071 (2016).
6. U. Kasavajjula, C. Wang and A. J. Appleby, *J. Power Sources*, **163**, 1003 (2007).
7. R. Teki, M. K. Datta, R. Krishnan, T. C. Parker, T. M. Lu, P. N. Kumta and N. Koratkar, *Small*, **5**, 2236 (2009).
8. H. Wu and Y. Cui, *Nano Today*, **7**, 414 (2012).
9. M. H. Park, M. G. Kim, J. Joo, K. Kim, J. Kim, S. Ahn, Y. Cui and J. Cho, *Nano Lett.*, **9**, 3844 (2009).
10. Q. Chen, R. Zhu, S. Liu, D. Wu, H. Fu, J. Zhu and H. He, *J. Mater. Chem. A.*, **6**, 6356 (2018).
11. V. Nulu, W. S. Kim and K. Y. Sohn, *Korean J. Chem. Eng.*, **36**, 1536 (2019).
12. P. Gao, X. Huang, Y. Zhao, X. Hu, D. Cen, G. Gao, Z. Bao, Y. Mei, Z. Di and G. Wu, *ACS Nano*, **12**, 11481 (2018).
13. A. Nulu, V. Nulu and K. Y. Sohn, *Sci. Adv. Mater.*, **12**, 337 (2020).
14. V. Nulu, W. S. Kim and T. Yu, *Korean J. Chem. Eng.*, **33**, 1500 (2016).
15. R. Patil, M. Phadatare, N. Blomquist, J. Örtegren, M. Hummelgård, J. Meshram, D. Dubal and H. Olin, *ACS Omega*, **6**, 10, 6600 (2021).
16. M. Su, S. Liu, H. Wan, A. Dou, K. Liu and Y. Liu, *Ionics*, **25**, 2103 (2019).
17. V. A. Nguyen and C. Kuss, *J. Electrochem. Soc.*, **167**, 065501 (2020).
18. Z. Xu, J. Yang, H. Li, Y. Nuli and J. Wang, *J. Mater. Chem. A*, **7**, 9432 (2019).
19. A. Nulu, V. Nulu and K. Y. Sohn, *ChemElectroChem.*, **7**, 4055 (2020).
20. M. Ashuri, Q. He, Y. Liu, K. Zhang, S. Emani, M. S. Sawicki, J. S. Shamie and L. L. Shaw, *Electrochim. Acta*, **215**, 126 (2016).
21. L. Y. Yang, H. Z. Li, J. Liu, Z. Q. Sun, S. S. Tang and M. Lei, *Sci. Rep.*, **5**, 10908 (2015).
22. D. L. Schulz, J. Hoey, J. Smith, A. Elangovan, X. Wu, I. Akhatov, S. Payne, J. Moore, P. Boudjouk, L. Pederson, J. Xiao and J. G. Zhang, *Electrochem. Solid State Lett.*, **13**, A143 (2010).
23. M.-H. Park, M. G. Kim, J. Joo, K. Kim, J. Kim, S. Ahn, Y. Cui and

J. Cho, *Nano Lett.*, **9**, 3844 (2009).
24. C. K. Chan, H. Peng and G. Liu, *Nat. Nanotechnol.*, **3**, 35 (2008).
25. M. D. Fleischauer, J. Li and M. J. Brett, *J. Electrochem. Soc.*, **156**, A33 (2009).
26. J. Xie, L. Tong, L. Su, Y. Xu, L. Wang and Y. Wang, *J. Power Sources*, **342**, 529 (2017).
27. Y. Park, N.-S. Choi, S. Park, S. H. Woo, S. Sim, B. Y. Jang, S. M. Oh, S. Park, J. Cho and K. T. Lee, *Adv. Energy Mater.*, **3**, 206 (2013).
28. M. Yoshio, T. Tsumura and N. Dimov, *J. Power Sources*, **146**, 14 (2005).
29. M. Jana and R. N. Singh, *Materialia*, **6**, 100314 (2019).
30. M. Ashuri, Q. He, Y. Liu, S. Emani and L. L. Shaw, *Electrochim. Acta*, **258**, 274 (2017).
31. V. Nulu and W. S. Kim, *Korean J. Chem. Eng.*, **32**, 1918 (2015).
32. A. Nulu, V. Nulu and K. Y. Sohn, *Korean J. Chem. Eng.*, **37**, 1795 (2020).
33. W. Wang, R. Epur and P. N. Kumta, *Electrochem. Commun.*, **13**, 429 (2011).
34. K. S. Park, K. M. Min, S. D. Seo, G. H. Lee, H. W. Shim and D. W. Kim, *Mater. Res. Bull.*, **48**, 1732 (2013).
35. L. Xiao, Y. H. Sehlleier, S. Dobrowolny, F. Mahlendorf, A. Heinzel, C. Schulz and H. Wiggers, *Mater. Today: Proceedings*, **4**, S263 (2017).
36. A. Gohier, B. Laïk, K. H. Kim, J. L. Maurice, J. P. P. Ramos, C. S. Cojocaru and P. T. Van, *Adv. Mater.*, **24**, 19 (2012).
37. L. F. Cui, L. Hu, J. W. Choi and Y. Cui, *ACS Nano*, **4**, 3671 (2010).
38. X. He, W. Zhao, D. Li, P. Cai, Q. Zhuang and Z. Ju. *New J. Chem.*, **43**, 18220 (2019).
39. Y. Gao, X. Qiu, X. Wang, X. Chen, A. Gu and Z. Yu, *Nanotechnology*, **31**, 155702 (2020).
40. Y. Ouyang, X. Zhu, F. Li, F. Lai, Y. Wu, Y.-E Miao and T. Liu, *Appl. Surf. Sci.*, **475**, 211 (2019).
41. X. Su, Q. L. Wu, J. C. Li, X. C. Xiao, A. Lott, W. Q. Lu, B. W. Sheldon and J. Wu, *Adv. Energy Mater.*, **4**, 1300882 (2014).
42. R. Epur, M. Ramanathan, M. K. Datta, D. H. Hong, P. H. Jampani, B. Gattu and P. N. Kumta, *Nanoscale*, **7**, 3504 (2015).
43. X. J. Feng, J. Yang, Y. T. Bie, J. L. Wang, Y. N. Nuli and W. Lu, *Nanoscale*, **6**, 12532 (2014).
44. R. Tarcan, O. T. Boer, I. Petrovai, C. Leordean, S. Astilean and I. Botiz, *J. Mater. Chem. C.*, **8**, 1198 (2020).
45. C. Botas, D. Carriazo, W. Zhang, T. Rojo and G. Singh, *Appl. Mater. Interfaces*, **8**, 28800 (2016).
46. J. G. Ren, C. Wang, Q. H. Wu, X. Liu, Y. Yang, L. He and W. Zhang, *Nanoscale*, **6**, 3353 (2014).
47. L. Xiao, Y. H. Sehlleier, S. Dobrowolny, H. Orthner, F. Mahlendorf, A. Heinzel, C. Schulz and H. Wiggers, *ChemElectroChem.*, **2**, 1983 (2015).
48. R. Cong, J. Y. Choi, J. B. Song, M. Jo, H. Lee and C. S. Lee, *Sci. Rep.*, **11**, 1283 (2021).
49. C. Weidenthaler, *Nanoscale*, **3**, 792 (2011).
50. S. M. Paek, E. Yoo and I. Honma, *Nano Lett.*, **9**, 72 (2009).
51. G. Fang, X. Deng, J. Zou and X. Zeng, *Int. J. Electrochem. Sci.*, **14**, 1580 (2019).
52. G. Fang, X. Deng, J. Zou and X. Zeng, *Electrochim. Acta*, **295**, 498 (2019).
53. F. Zhang, G. Zhu, K. Wang, X. Qian, Y. Zhao, W. Luo and J. Yang, *J. Mater. Chem. A.*, **7**, 17426 (2019).
54. L. Xue, G. Xu, Y. Li, S. Li, K. Fu, Q. Shi and X. Zhang, *ACS Appl. Mater. Interfaces*, **5**, 21 (2013).
55. W. Choi, H. C. Shin, J. M. Kim, J. Y. Choi and W. S. Yoon, *J. Electrochem. Sci. Technol.*, **11**, 1 (2020).
56. D. J. Xu, Y. X. Yao, G. Wegner, X. Fang, C. H. Chen and I. Lieberwirth, *Solid State Ion.*, **180**, 222 (2009).

Supporting Information

Unified NCNT@rGO bounded porous silicon composite as an anode material for Lithium-ion batteries

Arunakumari Nulu, Venugopal Nulu, Ji Seong Moon, and Keun Yong Sohn†

Department of Nanoscience and Engineering, Center for Nano Manufacturing, Inje University,
197 Inje-ro, Gimhae, Gyeongnam-do 50834, Korea
(*Received 28 December 2020 • Revised 26 March 2021 • Accepted 18 April 2021*)

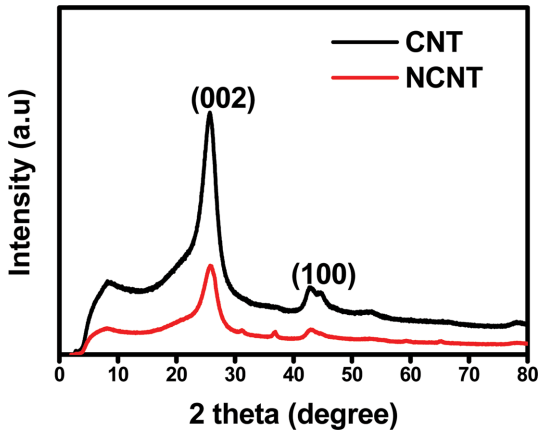

Fig. S1. XRD patterns of CNTs and N-doped CNTs.

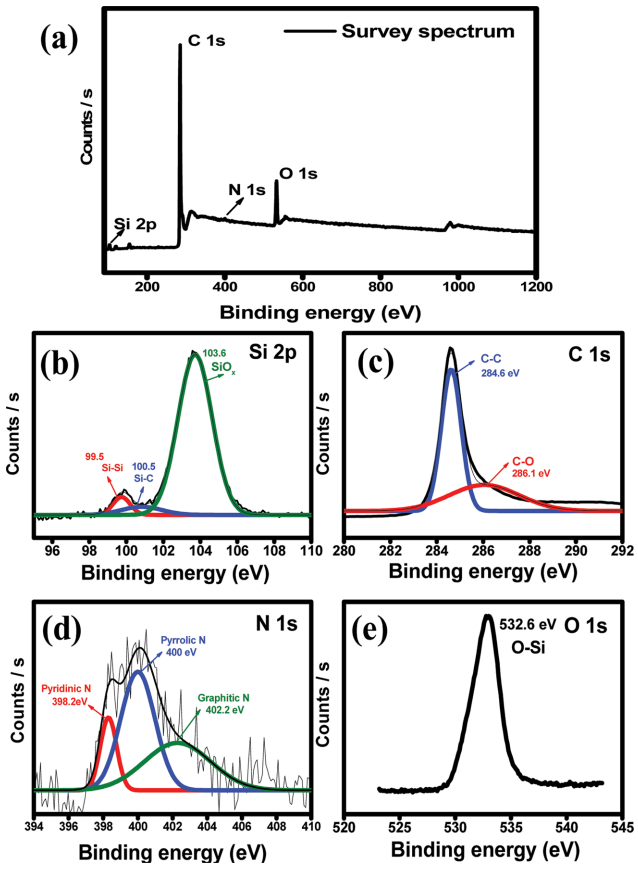

Fig. S2. XPS spectra of pSi/NCNT@rGO composite (a) survey scan spectra, (b) Si 2p, (c) C 1s, (d) N 1s, (e) O 1s.

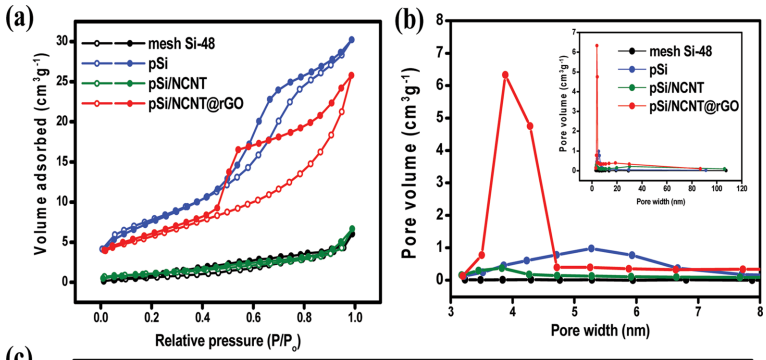

(c)

Sample	mesh Si-48	pSi	pSi/NCNT	pSi/NCNT@rGO
Pore volume (cm^3g^{-1})	0.009	0.275	0.228	0.902
BET surface area (m^2g^{-1})	2.548	163.694	90.175	442.292
Average pore width (nm)	3.132	5.274	3.827	3.882

Fig. S3. (a) N_2 adsorption and desorption isotherms, (b) pore size distribution curves of mesh Si-48, pSi, pSi/NCNT and pSi/NCNT@rGO (c) summarized values for pore volume, BET surface area, and average pore width of mesh Si-48, pSi, pSi/NCNT, and pSi/NCNT@rGO electrodes.

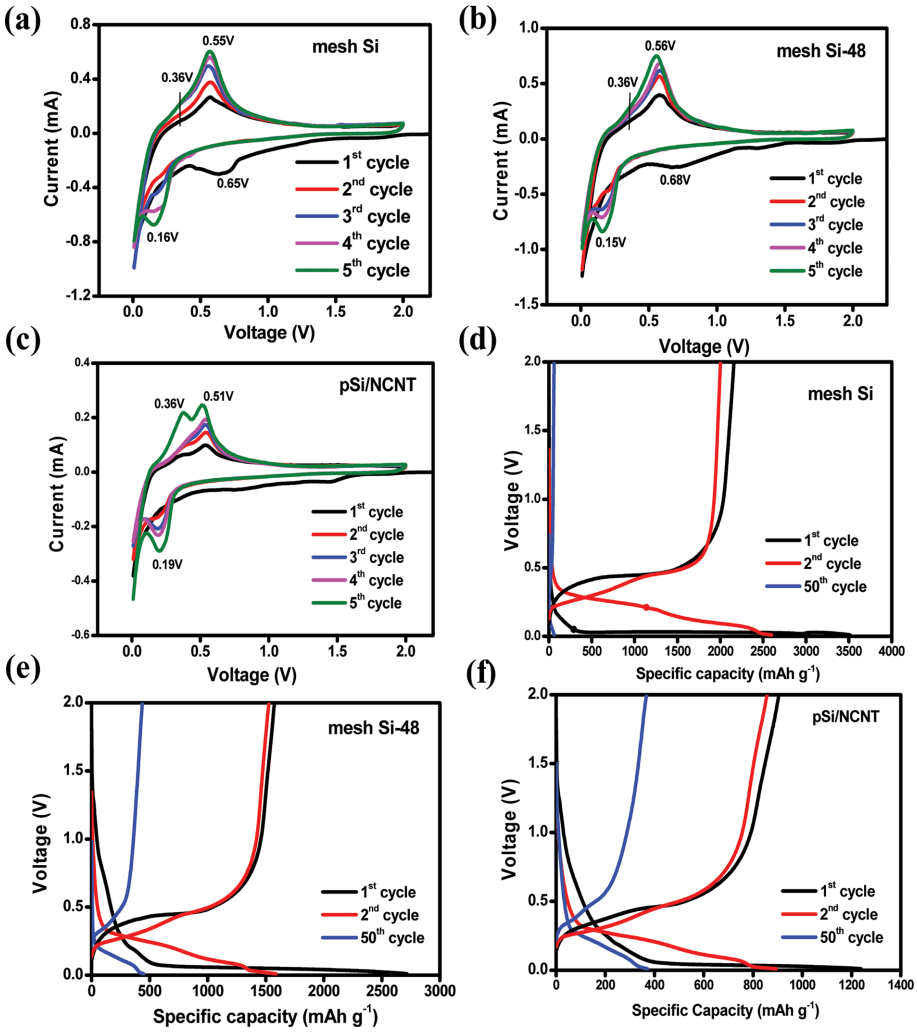

Fig. S4. Cyclic Voltammograms of (a) mesh Si, (b) mesh Si-48, (c) pSi/NCNT. Charge/discharge voltage profiles for the 1st, 2nd, and 50th cycles of (d) mesh Si, (e) mesh Si-48, (f) pSi/NCNT.

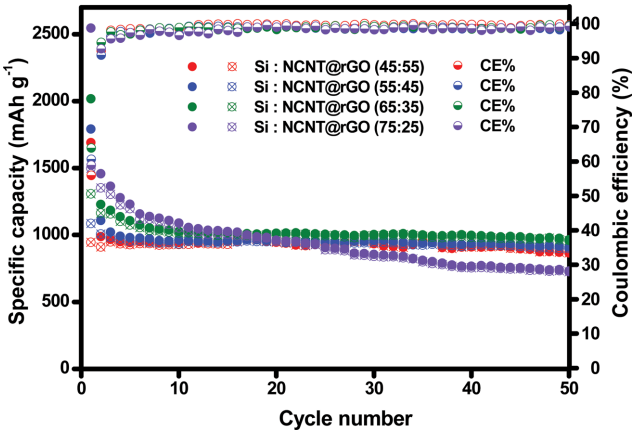

Fig. S5. Cyclability and coulombic efficiency results of pSi/NCNT@rGO composite electrodes at different pSi and NCNT@rGO ratios.

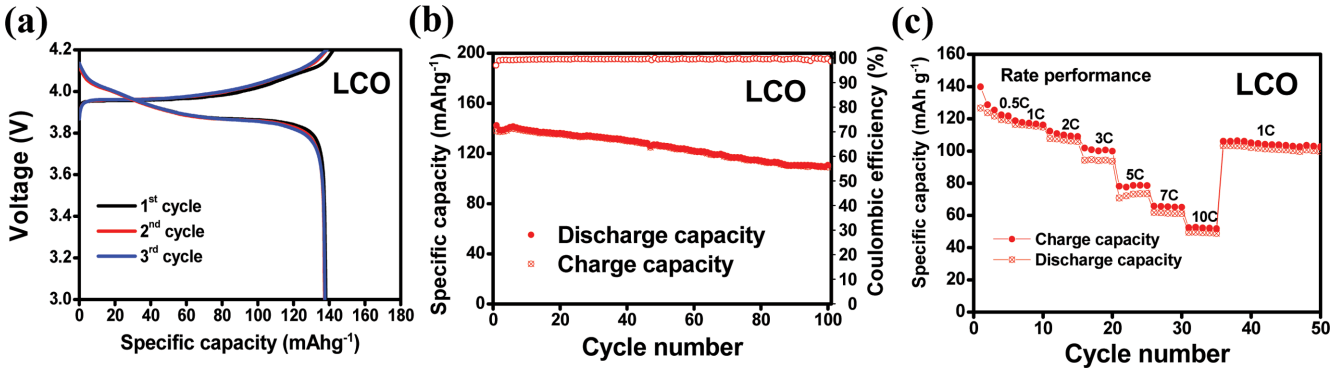

Fig. S6. $LiCoO_2$ half cell results (a) Charge/discharge voltage profiles (b) cyclability and coulombic efficiency (c) rate performance.